Cancer Nanotechnology

RESEARCH Open Access

Near-infrared modulated photothermal/nanozymatic dual-modal strategy for combating cancer via molybdenum selenide nanourchins

Yifan Li[1†], Chao Huang[2†], Zhengbin Wang[3†], Rui Tan[3†], Xianchun Fu[4*], Kaikai Xu[5], Qingsong Niu[3], Di Zhong[3], Mingyun Hong[6], Yanfeng Shi[7*] and Pengfei Zhang[3*]

†Yifan Li, Chao Huang, Zhengbin Wang and Rui Tan contributed equally to this work.

*Correspondence: 19863702285@163.com; shiyf19980622@163.com; pfzhang0106@163.com

[1] Department of Breast Center of the Affiliated Hospital of Qingdao University, Qingdao 266000, Shandong, China
[2] Institute of Biomedical Engineering, College of Medicine, Southwest Jiaotong University, Chengdu 610031, Sichuan, China
[3] Department of Urology, The First Affiliated Hospital of Anhui Medical University, Hefei 230022, Anhui, China
[4] Department of Urology, The Affiliated Hospital of Qingdao University, Qingdao 266003, Shandong, China
[5] Qingdao HIGHTOP Biotech Co., Ltd., Qingdao, China
[6] Hefei Maternal and Child Health Hospital, Hefei 230000, Anhui, China
[7] Jiangsu Key Laboratory for Nanotechnology and Collaborative Innovation Center of Advanced Microstructures, National Laboratory of Solid State Microstructures, Nanjing University, Nanjing 210093, People's Republic of China

Abstract

Background: Breast cancer, a major health concern globally, often faces challenges in the non-invasive elimination of cancer cells. This has prompted researchers to explore alternative strategies, such as photothermal therapy (PTT), which takes advantage of the location of breast cancer lesions. Additionally, the tumor microenvironment with high hydrogen peroxide (H_2O_2) provides a key prerequisite for treating tumors with nanozymes, especially those with peroxidase (POD)-like activity. However, the overexpression of TrxR1, which maintains redox homeostasis in tumor cells, limits reactive oxygen species (ROS)-based cytotoxic therapy. This study aims to present molybdenum selenide nano urchins ($MoSe_2$ NUs) with excellent photothermal conversion efficiency, POD-like activity and selective inhibition of TrxR1 to achieve photothermal enhanced nanocatalytic therapy for combating breast cancer.

Methods: The characterization of $MoSe_2$ NUs synthesized by the hydrothermal method was identified by TEM, XRD, Zeta potential and DLS. Whether MoSe2 NUs in conjunction with NIR possessed POD-like activities or not was identified via a TMB colorimetric method. The photothermal characteristics of $MoSe_2$ NUs excited by near-infrared were recorded by an infrared thermal imaging camera. The antitumor effect of $MoSe_2$ NUs was detected by cell death staining, apoptosis assay and animal experiments. TrxR1 and apoptosis-related protein expression were identified by Western blot and Immunohistochemistry.

Results: $MoSe_2$ NUs possessed excellent photothermal conversion efficiency, peroxidase (POD)-like activity, and selective inhibition of TrxR1. Furthermore, the photothermal effect of $MoSe_2$ NUs can enhance their POD-like activity, allowing for accurate cancer treatment under near-infrared (NIR) light. $MoSe_2$ NUs plus NIR and $MoSe_2$ NUs alone exhibited in vivo tumor inhibition rates of 69.7% and 35.1%, respectively. Mechanistically, NIR-regulated $MoSe_2$ NUs induced potent apoptosis of cancer cells by downregulating the TrxR1 and elevating intracellular ROS, thereby leading to caspase-3 cleavage.

Conclusions: This study demonstrated that $MoSe_2$ NUs under NIR irradiation can precisely and efficiently treat breast cancer and have great potential for clinical application.

Keywords: Cancer, $MoSe_2$, Photothermal therapy, Nanozyme, Apoptosis

Graphical Abstract

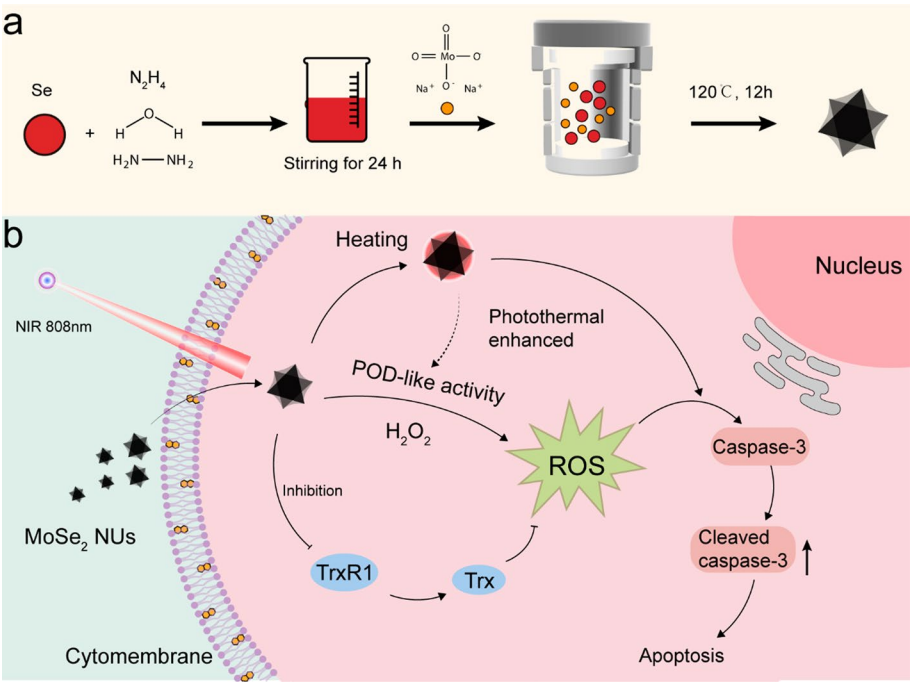

Introduction

Breast cancer (BC) is the most common malignancy among women. Since the 1980s, the global incidence rate has increased year by year (Siegel et al. 2023; Luo et al. 2022). The routine therapy of breast cancer covers surgery, radiotherapy, chemotherapy and other comprehensive treatments. However, radiotherapy and chemotherapy cannot eliminate local cancer cells due to limitations in chemotherapy tolerance (Tanwar et al. 2014; Liu et al. 2018). Therefore, this dilemma prompts experts and scholars to explore more effective alternative strategies (Hanafy 2021; Hanafy et al. 2021; Elsayed et al. 2021).Compared with traditional treatments, the location of breast cancer lesions provides a therapeutic window for near-infrared (NIR) photodynamic therapy.

In recent years, thermotherapy has been applied to treat cancer, but due to uncontrolled heating, burns occasionally occur. This photothermal regulated tumor treatment strategy is designed based on the principle of an NIR laser window in the range of 750 to 1000 nm, where the laser can penetrate several centimeters of body tissue without affecting the surface of normal skin (Chepurna et al. 2020; Jia et al. 2023). Moreover, NIR stimulated photodynamic therapy (PDT) has also become a potential anti-tumor treatment strategy. PDT with many advantages

for tumor elimination still has its limitations. The difficulty of photosensitizer delivery and the hypoxic microenvironment of malignant solid tumors greatly affect the treatment efficiency of PDT (Zou et al. 2020; Yang and Chen 2019; Lan et al. 2019; Alzeibak et al. 2021). Additionally, the aggravation of hypoxia may cause several adverse consequences, including radiation resistance, tumor invasiveness, angiogenesis, and tumor metastasis (McDonald et al. 2016).

However, the conventional high concentration of hydrogen peroxide (H_2O_2) and hypoxia in tumor microenvironment provides excellent conditions for nanozymatic tumor therapy rather than PDT (Hao et al. 2022). Among them, peroxidase can convert H_2O_2 within the tumor microenvironment into cytotoxic hydroxyl radicals, however natural peroxidase is unstable and difficult to deliver to the tumor microenvironment (Lu et al. 2022; Sadhu et al. 2024; Harshita and Park 2023). Whereas POD-like nanozymes have tunable, long-term storage, good stability, and tunable catalytic properties, making them an excellent alternative (Dong et al. 2022; Xu et al. 2022; Chen et al. 2023). The most common POD-active nanomaterials are Fe and Fe-based oxides, but they tend to lack photothermal absorption properties (Gao and Yan 2019). No further enhancement of POD could be achieved. Therefore, it is of great value to synthesize nanozymes that have both photothermal properties and the ability to regulate their own POD activity. Additionally, thioredoxin reductase 1 (TrxR1) protein is a key member of the thioredoxin (Trx) system that catalyzes the transfer of electrons from NADPH to Trx, converting it to a reduced state, thereby participating in a variety of reactions that maintain redox balance and is an important detoxification mechanism to protect cells from reactive oxygen species (ROS). TrxR1 protein is over-expressed in various tumors and is negatively correlated with the clinical prognosis of patients with tumors (Duan et al. 2014). Notably, several studies underscored that Se have the potential to promote the apoptosis of cancer cells through suppressing the expression of TrxR1 (Liu et al. 2012). Numerous studies highlighted that selenium-based nanoparticles inhibit the expression of TrxR1 in cancer cells through the formation of diselenides between TrxR1 and selenium (Liu et al. 2012; Purohit et al. 2017; Pan et al. 2020; Skogastierna et al. 2012). Thus, the effective inhibition of TrxR1 by selenium-based nanomaterials holds great potential for enhancing ROS-mediated antitumor therapy.

Herein, our synthesized molybdenum selenide nanourchins ($MoSe_2$ NUs) have excellent photothermal conversion efficiency, POD-like activity and good biocompatibility. In addition, the photothermal effect of the prepared $MoSe_2$ NUs regulates heat therapy and enhance their POD activity to kill cancer cells through NIR light, accurately treating cancer. Mechanistically, $MoSe_2$ induced an increase in intracellular ROS and downregulated the expression of TrxR1 in 4T1 cells, which in turn activated and cleaved caspase-3, an apoptotic executioner protein, while NIR light further cleaved caspase-3, which in turn enhanced the apoptosis-inducing ability of $MoSe_2$ NUs (Scheme 1).

Experimental section

Materials and biochemicals

Selenium powder, hydrazine hydrate, 3,3',5,5'-tetramethyl-benzidine (TMB) and sodium molybdate were bought from Macklin, China. The Calcein and PI were sourced from MedChemExpress. Fetal bovine serum (FBS) and Dulbecco's Modified Eagle Medium

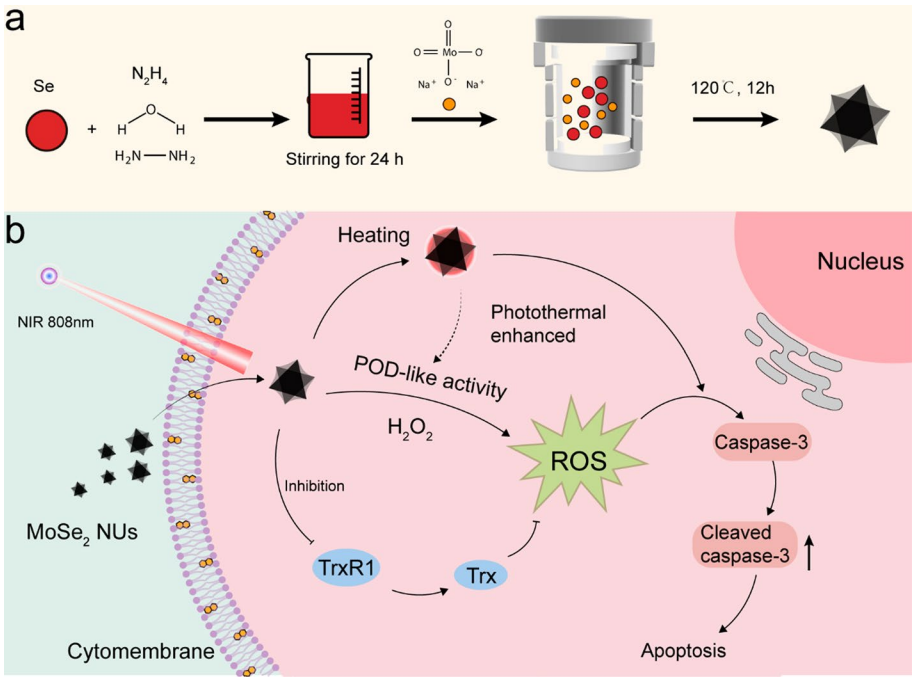

Scheme 1. Schematic diagram of $MoSe_2$ NUs synthesis route (**a**) and mechanism (**b**) of NIR-regulated nanozymatic/photothermal dual-modal therapy against breast tumor

(DMEM) were obtained from Procell. Additionally, we acquired 3-(4,5-dimethylthiazol-2-yl)-2,5-diphenyltetrazolium bromide (MTT) and the DCFH-DA probe from Sigma. The Annexin V-FITC/PI apoptosis assay kit was bought from Beijing Solarbio Science & Technology Co., Ltd. The antibodies for anti-TrxR1, and anti-Caspase-3 were obtained from CST and anti-GAPDH was purchased from Zen-Bio.

Synthesis of $MoSe_2$ NUs

The synthesis of $MoSe_2$ NUs was modified based on previous studies (Zhao et al. 2018) and divided into three processes. First, 2 mmol of selenium powder (Se) was weighed and dissolved in 10 mL hydrazine hydrate and sealed and stirred for 24 h to form the Se precursor solution. And then, 1 mmol of sodium molybdate (Na_2MoO_4) was weighed and dissolved in 20 mL pure water and stirred at room temperature for 40 mins to form the Mo precursor solution; Immediately, Se precursor solution was added to the Mo precursor solution, sonicated (300 W) for 15 min, and transferred to a 50 mL of hydrothermal reactor lined with polytetrafluoroethylene for 12 h; the heating temperatures were 120 ℃, respectively. At the end of the reaction, the $MoSe_2$ NUs were transferred to a beaker and first washed five times with deionized water after the hydrothermal kettle was cooled to room temperature. Finally, the $MoSe_2$ NUs were obtained and dried at 60 ℃ after washing with deionized water.

Characterization

Scanning electron microscopy (SEM) and transmission electron microscope (TEM) were employed to determine the nanomaterials' morphology. The crystal profile

characterization of $MoSe_2$ NUs was proved by an automatic X-ray diffractometer (XRD) equipped with CuKα radiation.

Peroxidase-mimic activity detection of $MoSe_2$ NUs

TMB and H_2O_2 as substrates were used to test the peroxidase (POD)-like catalytic activity of $MoSe_2$ NUs. The absorbance of oxidized TMB at 652 nm was measured and recorded after 10 min of reaction using a UV–Vis spectrophotometer. In detail, the kinetic curves of the acetate buffer solution being composed of TMB, H_2O_2 (100 mM) in the presence of MONDs, were determined by UV–Vis spectrophotometer, respectively.

Photothermal effect of $MoSe_2$ NUs

We irradiated $MoSe_2$ NUs at different concentrations (0, 20, 40, 60, 80, and 100 μg mL^{-1}) with an 808-nm NIR laser at 1.0 W/cm^2 and continuously recorded the temperature changes with an infrared (IR) thermal imaging camera. We also monitored temperature changes in tubes containing $MoSe_2$ NUs (100 μg mL^{-1}) at different laser power densities (0.8, 1.0, 1.2, 1.4, 1.6, and 1.8 W/cm^2). The photothermal conversion efficiency (PCE) was calculated based on the proposed algorithm after irradiating 100 μg/mL $MoSe_2$ NUs with a 1.0 W/cm^2 laser for 10 mins, followed by cooling for 20 mins (Chen et al. 2019).

Cytotoxicity assays and biocompatibility of $MoSe_2$ NUs

High concentrations of $MoSe_2$ NUs were sterilized by UV irradiation, and subsequently prepared into different concentrations of $MoSe_2$ NUs in DMEM which were added to 96-well plates. Following 24 h of culture in 4T1 and L929 cells, MTT was added and cell viability was measured 4 h later.

Detection of intracellular ROS

The intracellular ROS content was measured by DCFH-DA. Cells were seeded onto plates overnight, received different treatments, and were incubated for 4 h at 37 ℃. Next, 500 μL of DCFH-DA (10 μM) was added and incubated for 30 mins. Following washing with PBS, the intracellular fluorescence was captured with a fluorescence microscope.

Live/dead cell staining

4T1 cells were seeded in plates and subjected to various treatments. After the completion of treatment, the cells were washed for 2 times. 4T1 cells were stained with Calcein AM/PI and incubated at 37 °C for 30 mins. After incubation and washing, the live/dead 4T1 cells was observed with a fluorescence microscope.

Apoptosis assay

4T1 cells in 12-well plates were digested by washing twice with PBS after receiving different treatments. 4T1 cells were subsequently stained with (PI and Annexin V) for 15 mins. Subsequently, cellular fluorescence signals were quantified by flow cytometry. The sum of Q_2 and Q_3 was calculated as the apoptotic rate.

Statistical analysis

Statistical analysis and image processing were performed using Origin 2018 and SPSS 22.0. Data were tested for normality and presented as mean ± S.D.; the Student's t-test or One-way ANOVA was used to calculate the P-value, and further details were provided in figure legends.

Results and discussion

Characterizations

As presented in Fig. 1a,b, the SEM image and TEM image revealed the successful synthesis of $MoSe_2$ NUs with a sea urchin-like nanostructure uniformly distributed around 100 nm in size. Compared to structures such as nanodots, nanosheets, and nanospheres (Qi and Liu 2019; Yuwen et al. 2016; Liu et al. 2023; Wu et al. 2016), the sea urchin-like structure of $MoSe_2$ NUs may expose more oxygen vacancies and more easily exhibit enzyme activity(Zhou et al. 2023; Zhang et al. 2023). The image of $MoSe_2$ NUs were shown in Figure S1. Subsequently, we detected that the hydrodynamic diameter of $MoSe_2$ NUs was about 142 nm and the zeta potential was − 30.84 mV (Fig. 1c,d). The FT-IR spectrum of $MoSe_2$ NUs was shown in Figure S2, which is similar to previous study (Kailasa et al. 2023). The structural properties of the $MoSe_2$ NUs were investigated by XRD in the 2θ range from 20 to 80. Besides, the powder XRD pattern in Fig. 1e revealed that the peak of $MoSe_2$ NUs matched the reflections of crystallographic information (PDF # 29–0914). These results suggest that the $MoSe_2$ NUs has been successfully synthesized.

Photothermal effect and photostability of $MoSe_2$ NUs

Firstly, we investigated the photothermal effect of $MoSe_2$ NUs using an infrared thermal imaging camera. We found that as the concentration of $MoSe_2$ NUs increased, the

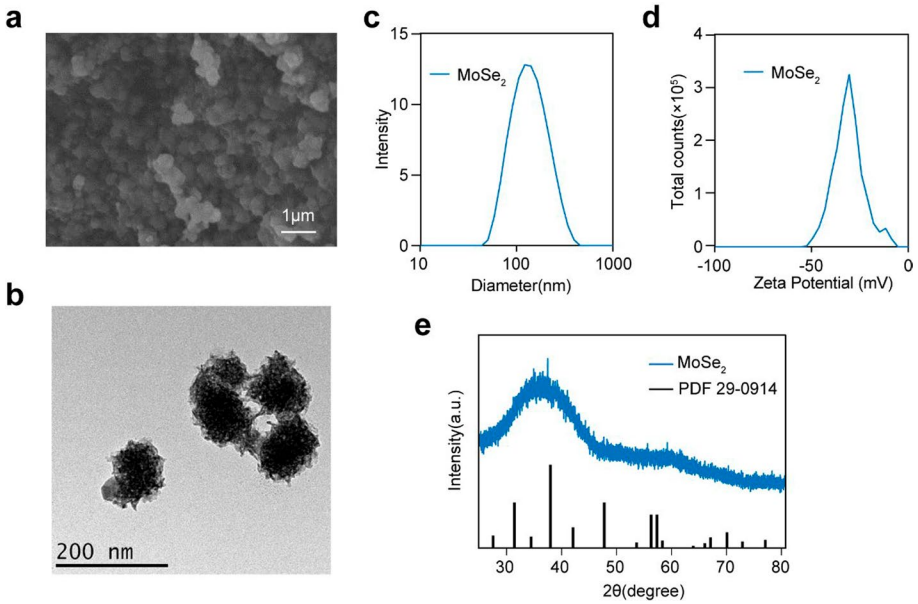

Fig. 1 a, **b** SEM (**a**) and TEM (**b**) of $MoSe_2$ NUs. **c**, **d** The DLS (**c**) and zeta potential (**d**) of $MoSe_2$ NUs. **e** The XRD of $MoSe_2$ NUs.

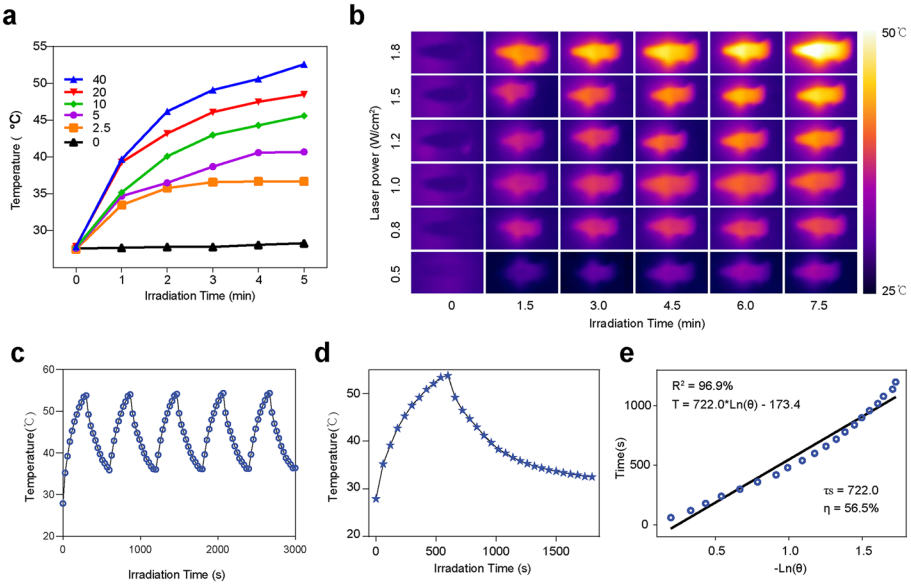

Fig. 2 **a** Temperature curves against time of Control (PBS) and $MoSe_2$ NUs with diverse concentrations (20–100 μg mL^{-1}) under 808 nm laser. **b** IR thermal images of $MoSe_2$ NUs with different laser power and irradiation time. **c** Five irradiation/cooling cycles of $MoSe_2$ NUs (100 μg mL^{-1}). **d** The photothermal profile of $MoSe_2$ NUs in PBS under NIR irradiation for 600 s and then NIR laser was switched off. **e** Linear time data versus −ln(θ) acquired from the cooling period of (**d**)

photothermal effect was significantly enhanced, indicating a close correlation between its photothermal effect and concentration. The time-dependent temperature curve is shown in Fig. 2a. The temperature of $MoSe_2$ NUs (100 μg mL^{-1}) rose to 52.6 ℃ and the increased temperature (ΔT) within 5 mins was up to 24.8 ℃. The temperature of $MoSe_2$ NUs with a concentration of 60 μg mL^{-1} can also reach 45.6 ℃ within 5 mins under laser irradiation. In addition, from the IR thermal image in Fig. 2b, the solution color changes from purple to yellow, and we can see that the photothermal effect of $MoSe_2$ NUs depends on the laser power. The temperature of the $MoSe_2$ NUs solution increases continuously with the increase of irradiation time and laser power.

When PBS served as the control group and was irradiated at the same power density, we observed only a marginal temperature increase of approximately 0.7 ℃. This suggests that the thermal effect of PBS alone remained largely unaffected. Typically, local heating of tumor cells to temperatures exceeding 45 ℃ can lead to complete tumor eradication. However, it's crucial to avoid excessively high temperatures, as they can potentially inflict severe damage to surrounding healthy tissues adjacent to the tumor. Taking these considerations into account, we determined that, in this study, a concentration of 80 μg mL^{-1} of $MoSe_2$ NUs was the most optimal choice for thermal ablation of tumor cells. This concentration resulted in a solution temperature precisely reaching 48.5 ℃, which is adequate for tumor cell ablation while minimizing harm to the surrounding normal tissue (Ding et al. 2021).

Subsequently, as shown in Fig. 2c, we further investigated the photothermal stability of $MoSe_2$ NUs by five irradiation/cooling cycles (one cycle includes heating for 5 mins and cooling for 5 mins). The photothermal conversion performance of $MoSe_2$ NU had little variation over five heating and cooling cycles. The photothermal conversion efficiency

(PCE) of $MoSe_2$ NUs was evaluated via recording the temperature changes of $MoSe_2$ NUs (100 μg mL^{-1}) during a 10-mins laser irradiation period (Fig. 2d). Detailed information regarding the PCE calculation is available in the Supporting Information. The calculated PCE for $MoSe_2$ NUs at a concentration of 100 μg mL^{-1} in PBS stands impressively high at 56.5%. Taken together, $MoSe_2$ NUs are excellent nanomaterials with good photothermal conversion efficiency and photostability.

The photothermal-enhanced POD activity of $MoSe_2$ NUs

To explore the peroxidase-like activity of the as-prepared $MoSe_2$ NUs, H_2O_2 and TMB were used as the substrates for the detection of the ultraviolet spectrum. Peroxidase has the capability to react with H_2O_2, leading to the generation of hydroxyl radicals (-OH). These -OH, in turn, facilitate the conversion of TMB into its oxidized form, resulting in the development of a distinct blue color characterized by a prominent peak at 652 nm. Figure 3a results indicated that neither $MoSe_2$ NUs nor H_2O_2 combined with TMB alone resulted in the generation of a blue color or any discernible UV–vis absorbance. Similarly, the combination of H_2O_2 with TMB did not produce weak absorption at 652 nm in the UV–vis spectrum. However, it's noteworthy that $MoSe_2$ NUs exhibited the ability to catalyze the oxidation of TMB in the presence of H_2O_2, resulting in the development of a blue aqueous solution characterized by an absorption peak at 652 nm.

The POD-like activity of $MoSe_2$ NUs at concentrations of 20 μg mL^{-1} with or without NIR light was also determined and is shown in Fig. 3b. After NIR light irradiation for 10 mins, the prominent peak of the $MoSe_2$ NUs + H_2O_2 + TMB + NIR was enhanced to the ≈2.05 fold of the $MoSe_2$ NUs + H_2O_2 + TMB. In summary, the results revealed that the $MoSe_2$ NUs possess POD-like activity, which can be boosted upon NIR irradiation.

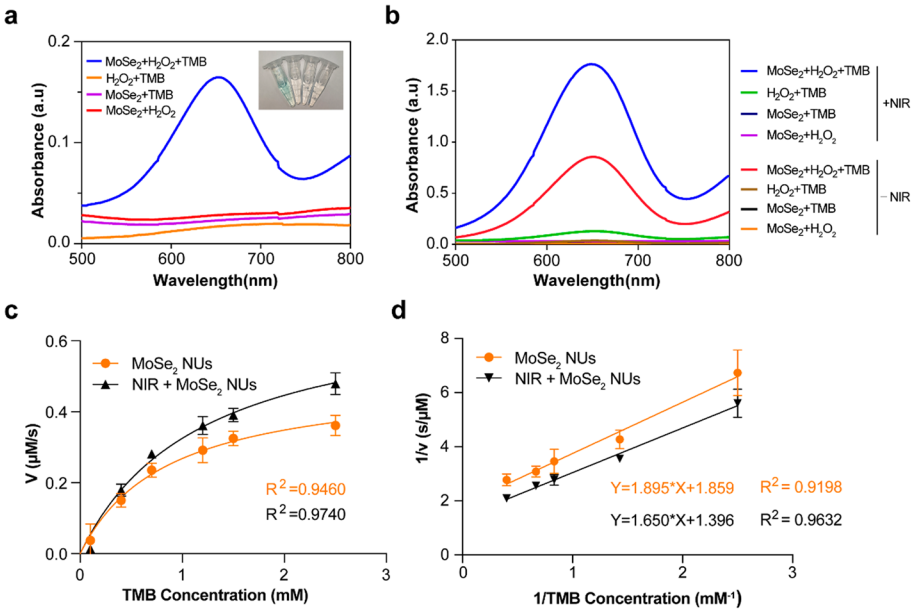

Fig. 3. **a** The POD-like activity of $MoSe_2$ NUs: the UV–vis spectra of the different treatments, the inset exhibited the corresponding image. **b** The POD-like activity of $MoSe_2$ NUs with or without NIR (808 nm, 1 W cm^{-2}). **c** The Michaelis–Menten kinetics fitting with initial rate [V] against TMB concentrations. **d** Corresponding Lineweaver–Burk plots of **c** (n = 3).

Correspondingly, we compared the enzyme kinetic parameters of $MoSe_2$ NUs with or without NIR. The maximum reaction rate (Vmax) and Michaelis Menten constant (Km) of $MoSe_2$ NUs with or without NIR against TMB were calculated according to the Lineweaver Burk plot. As shown in Fig. 3c, d, by plotting the initial rate of $MoSe_2$ NUs with or without NIR against different TMB concentrations, it was found that the reciprocal of the initial rate increases linearly with the reciprocal of TMB concentration. According to the Michaelis Equation, the Km and Vmax of $MoSe_2$ NUs for TMB are 1.019 mM and 5.38×10^{-8} M s^{-1}, respectively; while the Km and Vmax of $MoSe_2$ NUs + NIR for TMB are 1.182 mM and 7.16×10^{-8} M s^{-1}, respectively. These data confirmed that the $MoSe_2$ NUs + NIR system can serve as an effective catalyst, generating more -OH for tumor treatment compared to $MoSe_2$ NUs alone.

Photocytotoxicity and biocompatibility of $MoSe_2$ NUs

Since breast cancer is usually located in the skin, it is appropriate and feasible to treat 4T1 cells of breast cancer with NIR laser irradiation, so 4T1 cells are selected as the research object of these studies e (Tray et al. 2019; Li et al. 2022). In the context of cancer treatment strategies, assessing the biocompatibility and cytotoxicity of $MoSe_2$ NUs towards fibroblasts is fundamental for ideal nanomedicine. The MTT assay was employed to evaluate the cytotoxicity and biocompatibility of $MoSe_2$ NUs. Figure S3 illustrated the cell viability of both L929 and 4T1 cells cultured with varying concentrations of $MoSe_2$ NUs in DMEM for 24 h. Across the concentration range of 0 to 100 μg mL^{-1} of $MoSe_2$ NUs, the cell viability in both groups exceeded 90%, indicating minimal cytotoxicity and favorable biocompatibility of $MoSe_2$ NUs with L929 cells. Also, the uptake of $MoSe_2$ NUs in 4T1 cells was stronger than that in L929 (Figure S4). Furthermore, a dual-modal therapeutic approach combining photothermal therapy (PTT) and nanozymatic effects of $MoSe_2$ NUs on 4T1 cells was investigated. The cytotoxic effects on 4T1 cells induced by $MoSe_2$ NUs (80 μg mL^{-1}) with or without NIR (1.0 W/cm^2) were confirmed by staining 4T1 cells with Calcein-AM and PI. As depicted in Fig. 4a, compared to the Control group, the majority of 4T1 cells exhibited green fluorescence after incubation with either $MoSe_2$ NUs alone or under NIR irradiation (10 mins) alone, indicating that $MoSe_2$ NUs or laser irradiation alone were not effective in inactivating or treating 4T1 cells. A small amount of red fluorescence in the $MoSe_2$ NUs group indicated the relatively low cytotoxicity of $MoSe_2$ NUs toward cancer cells. In contrast, the PTT/Nanozymatic synergistic effect of $MoSe_2$ NUs resulted in nearly all 4T1 cells being inhibited when cultured with $MoSe_2$ NUs under NIR for 10 mins, as evident from the substantial red fluorescence observed in Fig. 4a. We further detected the apoptosis level of tumor cells after different treatments. The results in Fig. 4b revealed that the apoptotic rates in the Control and NIR groups (1.0 W/cm^2) were 9.70% and 9.84%, respectively. The treatment of $MoSe_2$ NUs (80 μg mL^{-1}) alone enhanced the apoptosis rate to 25.13%, while the apoptotic rates of $MoSe_2$ NUs + NIR groups rose to 61.02%. It reflected that NIR markedly enhanced the induction of apoptosis in 4T1 cells by $MoSe_2$ NUs.

As shown in Fig. 4c, we also quantitatively compared the cytotoxicity of different concentrations of $MoSe_2$ NUs with or without NIR (1.0 W/cm^2) on 4T1 cells and found that the cytotoxicity of $MoSe_2$ NUs + NIR was superior to that of $MoSe_2$ NUs treatment alone under different concentrations. The cell viability of $MoSe_2$ NUs and

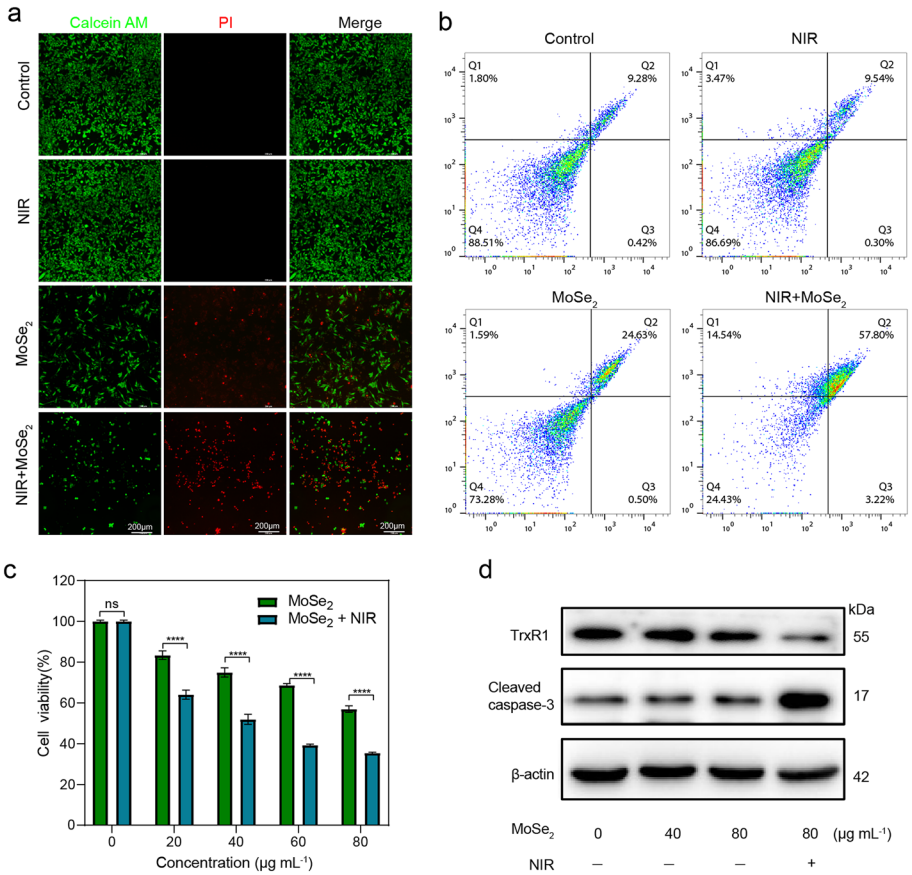

Fig. 4 **a** Fluorescence photographs of live and dead staining in 4T1 cells with different treatments. **b** The apoptosis rate of 4T1 cells with different treatments. **c** The cell viability of $MoSe_2$ NUs at various concentrations with or without NIR. **d** Immunoblot of TrxR1, cleaved caspase-3, and GAPDH expression in 4T1 cells with different treatments. (n = 3, mean ± S.D.; ns, no significant; ****P < 0.0001; one-way ANOVA)

$MoSe_2$ NUs + NIR at 80 μg mL^{-1} was 57.0% and 35.4%, respectively, with statistically significant differences. There is evidence that the TrxR1 protein, as a NADPH-dependent reductase of thioredoxin disulfide, is upregulated in various tumors and negatively correlated with the clinical prognosis of patients (Duan et al. 2014). Numerous studies highlighted that selenium-based nanoparticles, inhibit the expression of TrxR1 in cancer cells through the formation of diselenides between TrxR1 and selenium (Liu et al. 2012; Purohit et al. 2017; Pan et al. 2020; Skogastierna et al. 2012). Therefore, the expression of TrxR1 in 4T1 cells was further detected. As depicted in Fig. 4d, the expression of TrxR1 exhibited a decline corresponding to the increasing concentration of $MoSe_2$ NUs, and this decrease was even more pronounced when combined with NIR (1.0 W/cm^2), highlighting the potent inhibitory effect of $MoSe_2$ NUs + NIR on TrxR1. In parallel, we also examined cellular apoptosis at the molecular level. Caspase-3, a cysteine-aspartic acid protease, undergoes cleavage at an aspartate residue, resulting in the formation of p12 and p17 subunits, ultimately giving rise to cleaved Caspase-3, which plays a pivotal role in orchestrating the morphological changes associated with apoptosis (Hague et al. 2004). Also, the presence of $MoSe_2$ NUs treatment led to an upregulation of cleaved caspase-3, and this effect was further

enhanced when combined with NIR, indicating that $MoSe_2$ NUs induced a more pronounced level of apoptosis with the assistance of NIR.

Taking these results together, it can be concluded that NIR irradiation of $MoSe_2$ NUs can induce more apoptosis and downregulate the expression of TrxR1, exerting more effective proliferation suppression on 4T1 cancer cells than $MoSe_2$ NUs treatment alone.

ROS triggered by $MoSe_2$ NUs under NIR irradiation induces apoptosis in 4T1 cells

Further, given the apoptosis-inducing potential of photothermal treatment (Wang et al. 2018), we explore the possible mechanism of $MoSe_2$ NUs-induced apoptosis. In Fig. 5a, we detected intracellular ROS levels in 4T1 cells with different treatments by ROS probe 2',7'-Dichlorodihydrofluorescein diacetate (DCFH-DA). We found that the fluorescence intensity of 4T1 cells under NIR irradiation (1.0 W/cm^2) only was the same as that of the Control, while the fluorescence intensity of the $MoSe_2$ NUs (40 μg mL^{-1}) treatment group exhibited partial enhancement, while the green fluorescence of the NIR + $MoSe_2$ NUs group showed obvious enhancement compared to the $MoSe_2$ NUs group. To demonstrate ROS-induced cytotoxicity by $MoSe_2$ NUs, N-Acetyl-L-cysteine (NAC) and L-Glutathione reduced (GSH), as ROS scavengers, were applied to inhibit ROS (Hosseini et al. 2019; Niu et al. 2021). The results in Fig. 5b demonstrated that the addition of NAC and GSH could indeed inhibit the cytotoxicity of NIR + $MoSe_2$ NUs induced by ROS. Correspondingly, we detected the apoptotic protein cleaved caspase-3 and TrxR1.

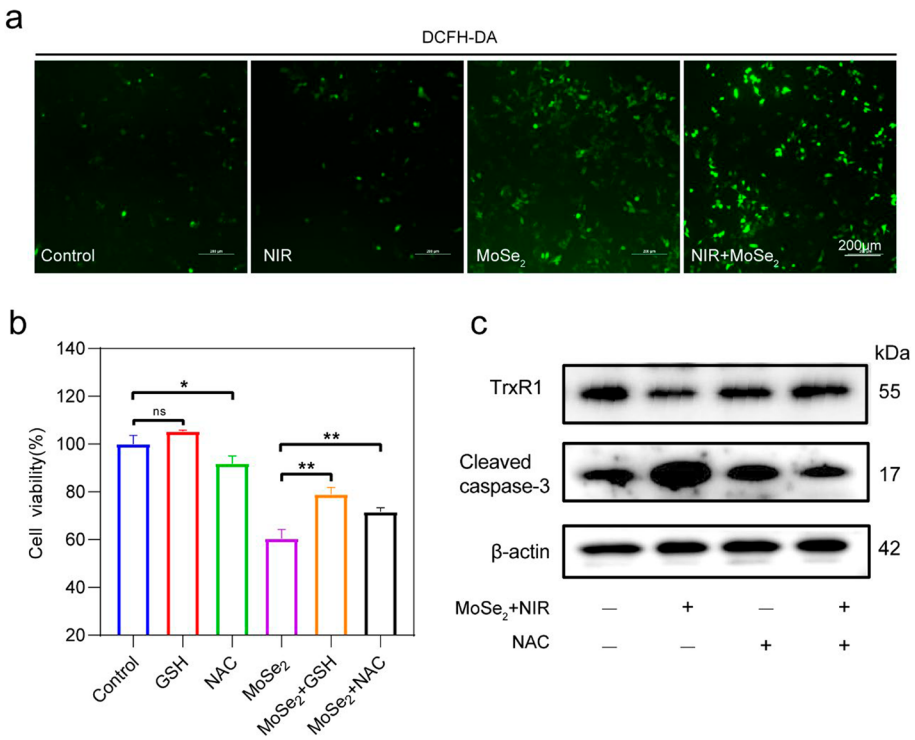

Fig. 5. **a** Fluorescence plots of 4T1 cells cultured with DCFH-DA after different treatments. **b** The cell viability of 4T1 cells with different treatments. **c** Immunoblot of TrxR1, cleaved caspase-3 and GAPDH expression of 4T1 cells with indicated treatments. (n = 3, mean ± S.D.; ns, no significant; *P < 0.05; **P < 0.01; one-way ANOVA)

As illustrated in Fig. 5c, the addition of ROS scavengers NAC caused a decrease in the expression of cleaved caspase-3 induced by $MoSe_2$ NUs + NIR, while the low-expression of TrxR1 by $MoSe_2$ NUs + NIR was almost unchanged. In summary, $MoSe_2$ NUs + NIR could downregulate TrxR1 and elicit the increase of ROS level, subsequently inducing apoptosis of 4T1 cells.

$MoSe_2$ NUs exert potent in vivo anti-tumor effects under NIR irradiation

Considering the excellent in vitro anti-tumor effect of $MoSe_2$ NUs under NIR, we further validated the combined therapy's in vivo anti-tumor effect. As shown in Fig. 6a, we first constructed 4T1 cell subcutaneous tumor-bearing mice and peritumorally injected

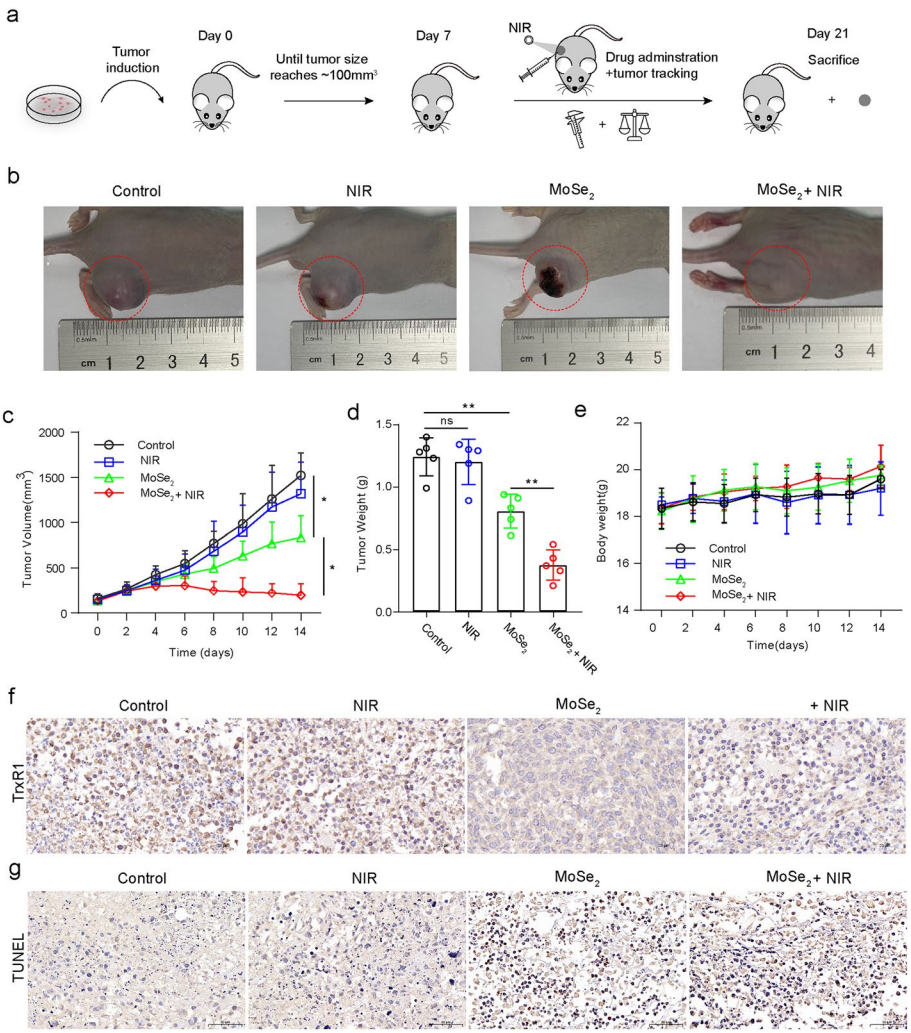

Fig. 6 In vivo assessment of the anti-tumor effect of $MoSe_2$ NUs treatment under NIR. **a** Illustration of the experimental procedure. **b** Photographic representations of tumors from tumor-bearing mice subjected to various treatment regimens. **c**, **d** Alterations in tumor volume **c** and tumor mass **d** within the tumor-bearing models of the specified groups. (n = 5, mean ± S.D.; ns, no significant; *P < 0.05; **P < 0.01; one-way ANOVA). **e**) Fluctuations in the body weight of tumor-bearing models undergoing different treatments. **f**, **g** Immunohistochemistry (IHC) analysis of xenografted tumor sections, showing immunostaining for TrxR1 (**f**), and TUNEL staining **g** in the indicated groups (n = 3). Scale bar: 50 μm (400×)

$MoSe_2$ NUs (4 mg kg^{-1}) every 2 days with or without NIR (1.0 W/cm^2). To assess the in vivo anti-tumor efficacy and biosafety, we monitored the tumor size and weight of 4T1 tumor-bearing mice every 2 days. After 14 days of treatment, the mice were euthanized, and the subcutaneous tumor tissue was removed and weighed. Representative images illustrating the tumor treatment outcomes for each group are presented in Fig. 6b. As depicted in Fig. 6c, the volume of tumors in the Control and NIR groups steadily increased, whereas the $MoSe_2$ NUs alone or $MoSe_2$ NUs + NIR treatment effectively reduced the tumor volume, the tumor volume treated with $MoSe_2$ NUs + NIR was lower than that treated with $MoSe_2$ NUs alone.

Furthermore, based on the excised tumor mass data shown in Fig. 6d, it is evident that $MoSe_2$ NUs + NIR treatment significantly inhibited tumor proliferation compared to the Control group, with an inhibition rate of 69.7%, which was higher than the inhibition rate observed with $MoSe_2$ NUs treatment alone (35.1% inhibition rate). Additionally, as demonstrated in Fig. 6e, the body weight of mice remained relatively stable across all groups, underscoring the favorable biosafety profile of both $MoSe_2$ NUs and $MoSe_2$ NUs + NIR with respect to mouse body weight. In addition, we also compared the expression of TrxR1 and Ki67 between the groups via Immunohistochemistry (IHC). As shown in Fig. 6f, both $MoSe_2$ NUs and $MoSe_2$ NUs + NIR reduced the expression of TrxR1, while the $MoSe_2$ NUs + NIR group had the lowest expression of TrxR1, demonstrating the TrxR1 inhibition effect of $MoSe_2$ NUs with or without NIR. Also, the results of TUNNEL staining are consistent with the expression of TrxR1, indicating that $MoSe_2$ NUs + NIR treatment has a stronger apoptotic induction effect in vivo (Fig. 6g). Of course, the in vivo biocompatibility of $MoSe_2$ NUs was also evaluated. As shown in Figure S5, no significant difference was observed in the important organs (heart, liver, spleen, lungs, and kidneys) between the two groups of mice, and the $MoSe_2$ NUs treatment did not cause significant toxic damage to the main organs. The biochemical analysis results also showed that there was no significant difference in liver and kidney function indicators between the $MoSe_2$ NUs treatment group and the control group (Figure S6). In summary, $MoSe_2$ NUs with good biosafety can effectively inhibit tumor progression in vivo.

Conclusions

In summary, the as-prepared $MoSe_2$ NUs with good biocompatibility had excellent photothermal conversion ability, photothermal-enhanced POD-like activity, and inhibition effect of TrxR1. Given this, $MoSe_2$ NUs under NIR irradiation could effectively produce cytotoxic OH− under single-wavelength laser irradiation, which in turn induces apoptosis. In addition, $MoSe_2$ NUs exhibited good photothermal stability. Surprisingly, $MoSe_2$ NUs still possess good PCE even after five heating and cooling cycles. Importantly, NIR irradiation could potentiate the POD-like activity of $MoSe_2$ NUs to ≈2.05 folds of $MoSe_2$ NUs only. While the apoptosis rate elicited by $MoSe_2$ NUs + NIR increased by 36% relative to $MoSe_2$ NUs only, and the $MoSe_2$ NUs + NIR induced more expression of cleaved caspase 3 than $MoSe_2$ NUs treatment alone. Notably, $MoSe_2$ NUs + NIR presented higher therapeutic efficacy on BC than $MoSe_2$ NUs alone, owing to PTT, inhibition of TrxR1, and photothermal-enhanced nanozymatic therapy. In conclusion, the combination of $MoSe_2$ NU-based PTT and photothermal-enhanced nanozyme therapy can

effectively improve the treatment of cancer cells, while its good biocompatibility makes it more potential for clinical application. This functional synergistic treatment paves a precise and efficient way for breast cancer treatment under near-infrared excitation.

Supplementary Information

The online version contains supplementary material available at https://doi.org/10.1186/s12645-024-00295-x.

Supplementary Material 1

Author contributions

Yifan Li: Analysis, Data curation, Writing- Original draft, Investigation, Drawing, Article revision. Chao Huang: Article revision, Data curation. Zhengbin Wang: Article revision, Data curation, Writing- Reviewing and Editing, Drawing. Rui Tan: Article revision, Data curation. Xianchun Fu: Writing, Review and editing. Kaikai Xu: Methodology. Drawing. Qingsong Niu: Methodology. Drawing. Di Zhong: Drawing. Mingyun Hong: Investigation, Article revision, Funding. Yanfeng Shi: Article revision, Writing, Review and editing. Pengfei Zhang: Writing, Supervision, Review and editing.

Funding

This study was supported by the Key Common Technology R & D Project of Hefei (GJ2022SM09).

Data availability

No datasets were generated or analysed during the current study.

Declarations

Ethics approval and consent to participate

All institutional and national guidelines for the care and use of laboratory animals were followed.

Competing interests

The authors declare no competing interests.

Received: 7 March 2024 Accepted: 23 October 2024
Published online: 04 November 2024

References

Alzeibak R, Mishchenko TA, Shilyagina NY, Balalaeva IV, Vedunova MV, Krysko DV, Targeting immunogenic cancer cell death by photodynamic therapy: past, present and future, J Immunother Cancer 2021;9(1).

Chen Z, Xia Q, Zhou Y, Li X, Qi L, Feng Q, Liu R, Chen W (2019) 2-Dicyanomethylenethiazole based NIR absorbing organic nanoparticles for photothermal therapy and photoacoustic imaging. J Mater Chem B 7(25):3950–3957

Chen J, Liu X, Zheng G, Feng W, Wang P, Gao J, Liu J, Wang M, Wang Q (2023) Detection of glucose based on noble metal nanozymes: mechanism, activity regulation, and enantioselective recognition. Small 19(8):e2205924

Chepurna OM, Yakovliev A, Ziniuk R, Nikolaeva OA, Levchenko SM, Xu H, Losytskyy MY, Bricks JL, Slominskii YL, Vretik LO, Qu J, Ohulchanskyy TY (2020) Core-shell polymeric nanoparticles co-loaded with photosensitizer and organic dye for photodynamic therapy guided by fluorescence imaging in near and short-wave infrared spectral regions. J Nanobiotechnology 18(1):19

Ding M, Shao K, Wu L, Jiang Y, Cheng B, Wang L, Shi J, Kong X (2021) A NO/ROS/RNS cascaded-releasing nano-platform for gas/PDT/PTT/immunotherapy of tumors. Biomater Sci 9(17):5824–5840

Dong H, Du W, Dong J, Che R, Kong F, Cheng W, Ma M, Gu N, Zhang Y (2022) Depletable peroxidase-like activity of Fe(3)O(4) nanozymes accompanied with separate migration of electrons and iron ions. Nat Commun 13(1):5365

Duan D, Zhang B, Yao J, Liu Y, Fang J (2014) Shikonin targets cytosolic thioredoxin reductase to induce ROS-mediated apoptosis in human promyelocytic leukemia HL-60 cells. Free Radical Biol Med 70:182–193

Elsayed AM, Sherif NM, Hassan NS, Althobaiti F, Hanafy NAN, Sahyon HA (2021) Novel quercetin encapsulated chitosan functionalized copper oxide nanoparticles as anti-breast cancer agent via regulating p53 in rat model. Int J Biol Macromol 185:134–152

Gao L, Yan X (2019) Nanozymes: biomedical applications of enzymatic Fe(3)O(4) nanoparticles from in vitro to in vivo. Adv Exp Med Biol 1174:291–312

Hague A, Eveson JW, MacFarlane M, Huntley S, Janghra N, Thavaraj S (2004) Caspase-3 expression is reduced, in the absence of cleavage, in terminally differentiated normal oral epithelium but is increased in oral squamous cell carcinomas and correlates with tumour stage. J Pathol 204(2):175–182

Hanafy NAN (2021) Optimally designed theranostic system based folic acids and chitosan as a promising mucoadhesive delivery system for encapsulating curcumin LbL nano-template against invasiveness of breast cancer. Int J Biol Macromol 182:1981–1993

Hanafy NAN, Leporatti S, El-Kemary MA (2021) Extraction of chlorophyll and carotenoids loaded into chitosan as potential targeted therapy and bio imaging agents for breast carcinoma. Int J Biol Macromol 182:1150–1160

Hao Y, Gao Y, Fan Y, Zhang C, Zhan M, Cao X, Shi X, Guo R (2022) A tumor microenvironment-responsive poly(amidoamine) dendrimer nanoplatform for hypoxia-responsive chemo/chemodynamic therapy. J Nanobiotechnology 20(1):43

Harshita TJ, Park SK (2023) Kailasa, Microwave-assisted synthesis of green fluorescent copper nanoclusters: a novel approach for sensing of hydroxyl radicals and pyrophosphate ions via a "turn-off–on" mechanism. New J Chem 47(43):20038–20047
Hosseini E, Ghasemzadeh M, Atashibarg M, Haghshenas M (2019) ROS scavenger, N-acetyl-l-cysteine and NOX specific inhibitor, VAS2870 reduce platelets apoptosis while enhancing their viability during storage. Transfusion 59(4):1333–1343
Jia T, Guan ZJ, Zhang C, Zhu XZ, Chen YX, Zhang Q, Yang Y, Sun D (2023) Eight-electron superatomic Cu(31) nanocluster with chiral kernel and NIR-II emission. J Am Chem Soc 145(18):10355–10363
Kailasa SK, Vajubhai GN, Koduru JR, Park TJ (2023) Recent progress of nanomaterials for colorimetric and fluorescence sensing of reactive oxygen species in biological and environmental samples. Trends Environ Anal Chem 37:e00196
Lan M, Zhao S, Liu W, Lee CS, Zhang W, Wang P (2019) Photosensitizers for photodynamic therapy. Adv Healthc Mater 8(13):e1900132
Li Y, Zhang H, Merkher Y, Chen L, Liu N, Leonov S, Chen Y (2022) Recent advances in therapeutic strategies for triple-negative breast cancer. J Hematol Oncol 15(1):121
Liu Y, Li Y, Yu S, Zhao G (2012) Recent advances in the development of thioredoxin reductase inhibitors as anticancer agents. Curr Drug Targets 13(11):1432–1444
Liu L, Xie HJ, Mu LM, Liu R, Su ZB, Cui YN, Xie Y, Lu WL (2018) Functional chlorin gold nanorods enable to treat breast cancer by photothermal/photodynamic therapy. Int J Nanomed 13:8119–8135
Liu G, Yan C, Sui X, Kuang D (2023) Combined simulation and experimental study on spectral absorbance of partially disordered MoSe(2)nanospheres. Nanotechnology 34(40):405704
Lu H, Xu S, Ge G, Guo Z, Zhao M, Liu Z (2022) Boosting chemodynamic therapy by tumor-targeting and cellular redox homeostasis-disrupting nanoparticles. ACS Appl Mater Interfaces 14(39):44098–44110
Luo J, Zou H, Guo Y, Tong T, Ye L, Zhu C, Deng L, Wang B, Pan Y, Li P (2022) SRC kinase-mediated signaling pathways and targeted therapies in breast cancer. BCR 24(1):99
McDonald PC, Chafe SC, Dedhar S (2016) Overcoming hypoxia-mediated tumor progression: combinatorial approaches targeting pH regulation angiogenesis and immune dysfunction. Front Cell Dev Biol 4:27
Niu B, Liao K, Zhou Y, Wen T, Quan G, Pan X, Wu C (2021) Application of glutathione depletion in cancer therapy: enhanced ROS-based therapy, ferroptosis, and chemotherapy. Biomaterials 277:121110
Pan S, Yang J, Ji S, Li T, Gao S, Sun C, Xu H (2020) Cancer therapy by targeting thioredoxin reductase based on selenium-containing dynamic covalent bond. CCS Chemistry 2(3):225–235
Purohit MP, Verma NK, Kar AK, Singh A, Ghosh D, Patnaik S (2017) Inhibition of thioredoxin reductase by targeted selenopolymeric nanocarriers synergizes the therapeutic efficacy of doxorubicin in MCF7 human breast cancer cells. ACS Appl Mater Interfaces 9(42):36493–36512
Qi F, Liu R (2019) Tumor-targeted and biocompatible MoSe(2) nanodots@albumin nanospheres as a dual-modality therapy agent for synergistic photothermal radiotherapy. Nanoscale Res Lett 14(1):67
Sadhu VA, Jha S, Park TJ, Kailasa SK (2024) Green emissive molybdenum nanoclusters for selective and sensitive detection of hydroxyl radical in water samples. J Fluoresc. https://doi.org/10.1007/s10895-023-03578-5
Siegel RL, Miller KD, Wagle NS, Jemal A (2023) Cancer statistics, 2023. CA Cancer J Clin 73(1):17–48
Skogastierna C, Johansson M, Parini P, Eriksson M, Eriksson LC, Ekström L, Björkhem-Bergman L (2012) Statins inhibit expression of Thioredoxin reductase 1 in rat and human liver and reduce tumour development. Biochem Biophys Res Commun 417(3):1046–1051
Tanwar J, Das S, Fatima Z, Hameed S (2014) Multidrug resistance: an emerging crisis. Interdiscip Perspect Infect Dis 2014:541340
Tray N, Taff J, Adams S (2019) Therapeutic landscape of metaplastic breast cancer. Cancer Treat Rev 79:101888
Wang Y, Zhang F, Wang Q, Yang P, Lin H, Qu F (2018) Hierarchical MoSe(2) nanoflowers as novel nanocarriers for NIR-light-mediated synergistic photo-thermal/dynamic and chemo-therapy. Nanoscale 10(30):14534–14545
Wu Y, Xu M, Chen X, Yang S, Wu H, Pan J, Xiong X (2016) CTAB-assisted synthesis of novel ultrathin MoSe2 nanosheets perpendicular to graphene for the adsorption and photodegradation of organic dyes under visible light. Nanoscale 8(1):440–450
Xu D, Wu L, Yao H, Zhao L (2022) Catalase-like nanozymes: classification, catalytic mechanisms, and their applications. Small 18(37):e2203400
Yang Z, Chen X (2019) Semiconducting perylene diimide nanostructure: multifunctional phototheranostic nanoplatform. Acc Chem Res 52(5):1245–1254
Yuwen L, Zhou J, Zhang Y, Zhang Q, Shan J, Luo Z, Weng L, Teng Z, Wang L (2016) Aqueous phase preparation of ultrasmall MoSe2 nanodots for efficient photothermal therapy of cancer cells. Nanoscale 8(5):2720–2726
Zhang J, Yang Y, Qin F, Hu T, Zhao X, Zhao S, Cao Y, Gao Z, Zhou Z, Liang R, Tan C, Qin Y (2023) Catalyzing generation and stabilization of oxygen vacancies on CeO(2–x) nanorods by Pt nanoclusters as nanozymes for catalytic therapy. Adv Healthc Mater. https://doi.org/10.1002/adhm.202302056
Zhao X, Zhao Y, Liu Z, Yang Y, Sui J, Wang H-E, Cai W, Cao G (2018) Synergistic coupling of lamellar MoSe2 and SnO2 nanoparticles via chemical bonding at interface for stable and high-power sodium-ion capacitors. Chem Eng J 354:1164–1173
Zhou P, Wang Z, Chen H, Yu D, Dai C, Qiu Z, Gao F, Pan B, Yuan F (2023) Oxygen vacancy-enhanced catalytic activity of hyaluronic acid covered-biomineralization nanozyme for reactive oxygen species-augmented antitumor therapy. Int J Biol Macromol 236:124003
Zou J, Zhu J, Yang Z, Li L, Fan W, He L, Tang W, Deng L, Mu J, Ma Y, Cheng Y, Huang W, Dong X, Chen X (2020) A phototheranostic strategy to continuously deliver singlet oxygen in the dark and hypoxic tumor microenvironment. Angew Chem Int Ed 59(23):8833–8838

Publisher's Note